Multi-physics modelling of molten pool development and track formation in multi-track, multi-layer and multi-material selective laser melting

Heng Gu[a*], Chao Wei[b], Lin Li[b], Quanquan Han[a], Rossitza Setchi[a*], Michael Ryan[a], Qian Li[b]

[a] Cardiff School of Engineering, Cardiff University, Cardiff CF24 3AA, UK

[b] Laser Processing Research Centre, School of Mechanical, Aerospace and Civil Engineering,
  The University of Manchester, Manchester M13 9PL, UK

Email: GuH5@cardiff.ac.uk, Setchi@cardiff.ac.uk

Abstract

Selective laser melting (SLM) is a promising powder-based additive manufacturing technology due to its capability to fabricate metallic components with complex geometries. While most previous investigations focus on printing with a single material, recent industry-oriented studies indicate the need for multi-material SLM in several high-value manufacturing sectors including medical devices, aerospace and automotive industries. However, understanding the underlying physics in multi-material SLM remains challenging due to the difficulties of experimental observation. In this paper, an integrated modelling framework for multi-track, multi-layer and multi-material SLM is developed to advance the in-depth understanding of this process. The main novelty is in modelling the molten pool evolvement and track morphology of multiple materials deposited on the same and across different layers. Discrete element method (DEM) is employed to reproduce the powder deposition process of multiple materials in different deposition patterns, with particle size distribution imported from a particle size analyser. Various phenomena including balling effect, keyhole depression, and lack of fusion between layers are investigated with different laser energy inputs. As a result of the different thermal properties, several process parameters including energy density and hatch spacing are optimised for different powder materials to obtain a continuous track profile and improved scanning efficiency. The interface between two layers of different materials is visualised by simulation; it was found that the phase migration at the interface is related to the convection flow inside the molten pool, which contributes to the mixing of the two materials and elemental diffusion. This study significantly contributes to the challenging area of multi-material additive manufacturing by providing a greater in-depth understanding of the SLM process from multi-material powder deposition to laser interaction with powders across multiple scanning tracks and different building layers than can be achieved by experimentation alone.

Keywords: Selective laser melting (SLM); Multi-material; Heat transfer; Discrete element method (DEM); Computational fluid dynamics (CFD); Additive manufacturing

1.Introduction

Selective laser melting (SLM) is a powder-based additive manufacturing process which uses a high power-density laser to melt and fuse powders layer-by-layer to form a three-dimensional part [1]. SLM has many advantages over other conventional manufacturing methods in terms of design flexibility, material usage and manufacturing cycle time [2, 3]. Components of a wide variety of materials including metal alloys and metal based composites can be successfully produced by SLM [4, 5]. Despite this, attention is currently focused on printing each designed part with single material at a time. Recently, there has been growing interest in the investigation of multi-material SLM due to its great potential for some specific applications where different material properties are required at different locations of the directly manufactured parts.

Efforts have been made to develop multi-material SLM systems which enable the printing of multiple materials across different layers as well as on the same building layer. A double powder spreading SLM system was developed by Demir and Previtali [6] to manufacture multi-graded components by gradually controlling the construction of two materials (Fe/Al-12Si). Liu et al. [7] applied a powder dispensing technique to deliver two powder materials in SLM and bimetallic laminates of 316L/C18400 with good metallurgical bonding at the interface were produced. Other bimetallic structures of AlSi10Mg/ C18400 [8] and CuSn/18Ni300 [9] were also successfully manufactured using multi-material SLM, with multiple materials processed across different layers. A big challenge for multi-material SLM lies in realizing the powder deposition of different materials on the same building layer with required deposition patterns. To achieve this, Wei et al. [10, 11] demonstrated a multi-material SLM system which combined conventional powder-bed spreading with point-by-point multiple material selective powder removal and point-by-point dry powder delivery techniques. By adopting this system, Wei et al. [12] embedded anti-counterfeiting safety features (a QR code made of Cu10Sn) into metallic components made of 316L. A functionally graded 316L/Cu10Sn component [13] was also manufactured using this system, which can be applied to nuclear power plants and heavy electronics where both high stiffness and good thermal/electrical conductivity are required.

Considering that all the complex physical phenomena in SLM occur at microsecond and micrometer scales, it is challenging to conduct real-time observation during experiments to obtain a comprehensive understanding of the process. Alternatively, numerical simulations have been employed to help investigate the complicated mechanisms and predict the formation of defects in SLM. For single-track/singe-layer SLM processes, the significant effects of recoil

pressure and Marangoni convection on the formation of denudation, pores and spatter have been studied by developing multi-physics CFD models [14, 15, 16]. Some other phenomena including vaporization, balling occurrence and keyhole formation were examined by investigating the effect of laser energy density with the help of modelling [17, 18, 19]. The microstructure evolution during SLM has been revealed by coupling thermal fluid dynamics and microstructure analysis using phase field modelling [20] and cellular automata [21, 22]. Apart from single-track/singe-layer SLM, studies have been extended to examine the multi-track and/or multi-layer powder bed fusion processes. The formation of near-spherical and irregularly shaped defects during multi-layer SLM process have been studied by adopting high-fidelity powder scale models [23, 24]. The influence of layer thickness and surface unevenness on solidified tracks were examined [25, 26]. In addition, the formation of balling effect, track nonuniformity and inter-track/interlayer voids were also investigated by understanding the effects of hatch spacing and scanning strategy [27, 28]. Despite some good understanding of multi-track and multi-layer SLM processes has been achieved by modelling, all the mentioned studies only focus on simulating SLM with one single powder material. For multi-material SLM, Tan et al. [29] made the first attempt to model the multi-material process by adopting Molecular Dynamic method. However, many assumptions were made in their model, which did not consider most of the physics involved in SLM, including surface tension forces, multi-phase flow and molten pool formation. Thus, the model does not reveal the complexity of the process especially when materials of very different thermal properties are included. Apart from CFD modelling of the molten pool development, powder bed simulation for SLM has also been extensively investigated by using discrete element method (DEM) [30, 31, 32, 33]. However, all the studies are based on modelling the powder deposition with one single material.

Despite the rapid development of multi-material SLM systems, there have been no scientific publications on investigating the molten pool development and track formation during multi-material SLM processes, and thus the underlying physics of multi-material SLM remains unknown. In addition, no work has been found on simulating powder bed deposition of multiple materials on the same building layer and across different layers with different patterns.

In this study, an integrated modelling framework including multi-material powder deposition and laser-powder interaction is developed to simulate the multi-track, multi-layer and multi-material SLM process of 316L and Cu10Sn powders. Process parameters are varied to examine the effect of energy density on various phenomena which occur in SLM, including balling effect, keyhole depression and lack of fusion. The development of temperature histories

and molten pool volumes is used to compare the fluid-dynamics inside the molten pool for two powder materials with different thermal properties, on the same building layer and across different layers. The simulated interface between two layers of different materials is compared with experimental results and the effect of convection flow inside the molten pool on the phase migration at the interface is studied.

2. Modelling framework and methodology

2.1 Integrated modelling framework

Fig. 1 presents the computational framework for multi-physics modelling. As shown, the powder size distribution of different powders is first examined using a particle size analyser (Malvern Mastersize 3000). Based on these results, DEM is employed to generate a distribution of particles and initialise the powder deposition for the first scanning layer. The powder information is then transferred to a CFD model to examine the interaction between the laser beam and the powder, which includes the calculation of multi-phase flow, surface tension forces, melting and solidification, gravitational force, recoil pressure and a self-adaptive Gaussian heat source. After obtaining the temperature distribution and profile of the scanned track, the geometry of the solidified powder bed is transferred back to DEM to initialise the powder deposition of the second layer. These steps are repeated to enable the investigation of molten pool development and track formation for multi-material deposition on the same building layer and across different layers scanned with multiple tracks.

<Insert Figure 1>

2.2 Modelling of powder deposition process

The discrete element method (DEM) is employed to simulate the deposition of the powders. Hertz-Mindlin with JKR cohesion model [34] is implemented to calculate the translational and rotational motions of the powder. The normal force F_n and tangential force F_t are given using equations (1) and (2) [34]

$$F_n = \frac{4}{3}E^*\sqrt{R^*}\delta_n^{3/2} - 2\sqrt{\frac{5}{6}}\frac{lne}{\sqrt{ln^2e+\pi^2}}(2E^*\sqrt{R^*\delta_n}m^*)^{1/2}\overrightarrow{v_n^{rel}} \qquad (1)$$

$$F_t = -8G^*\sqrt{R^*\delta_n}\delta_t - 2\sqrt{\frac{5}{6}}\frac{lne}{\sqrt{ln^2e+\pi^2}}(8G^*\sqrt{R^*\delta_n}m^*)^{1/2}\overrightarrow{v_t^{rel}} \qquad (2)$$

where E^* is the equivalent Young's Modulus, R^* is the equivalent radius, δ_n is the normal overlap, m^* is the equivalent mass, e is the coefficient of restitution, $\overrightarrow{v_n^{rel}}$ is the normal component of the relative velocity, δ_t is the tangential overlap, G^* is the equivalent shear modulus and $\overrightarrow{v_t^{rel}}$ is the tangential component of the relative velocity. Rolling friction, τ_i, is considered by applying a torque to the contacting surfaces, as shown in equation (3) [34]:

$$\tau_i = -\mu_r F_n R_i \omega_i \qquad (3)$$

where μ_r is the coefficient of rolling friction, R_i is the distance of the contact point from the particle centre and ω_i is the unit angular velocity vector of the particle. The cohesion force between the powders is calculated using equation (4) [35]

$$F_{JRK} = -4\sqrt{\pi\gamma E^*}a^{3/2} + \frac{4E^*}{3R^*}a^3 \qquad (4)$$

The commercial software EDEM v2019 [34] is used to perform the multi-material powder deposition simulations. The two powder materials used to simulate multi-track, multi-layer and multi-material processes are 316L stainless steel and Cu10Sn, which allows a comparison between the model and experimental results. The combination of stainless steel and copper alloy has been extensively used in many industries, such as power generation, nuclear energy and heavy electronics, due to their complementary properties including good corrosion resistance of stainless steel and excellent thermal and electrical conductivities of copper alloy [36, 37]. The 316L stainless steel powder examined in the particle analysis and used in the SLM experiments, was supplied by LPW Technology Ltd. UK. The Cu10Sn powder was provided by Makin Metal Powders Ltd. UK. The morphologies of these two powders are shown in Fig. 2(a) and Fig. 2(b); the images were taken by a scanning electron microscope (SEM). The particle size distributions shown in Fig. 2(c) and Fig. 2(d) were examined by Malvern UK Mastersizer 3000 particle size analyser. The powder sizes of D_{10}, D_{50} and D_{90} were measured as 17.9, 30.3 and 50 µm for 316L, and 9.79, 22.4 and 39.5 µm for Cu10Sn, respectively. The obtained powder distributions were imported into EDEM as normal distribution functions. After calculation, the simulated powder sizes of D_{10}, D_{50} and D_{90} were found to be 16.1, 28.2 and 48.4 µm for 316L, and 8.5, 20.7 and 36.9 µm for Cu10Sn. Fig. 2(c) and Fig. 2(d) show the simulated powder size distributions compared to the measured results for the two powders. To simulate the powder deposition process, powders are first generated from a plane above the

substrate with required layer thickness and then fall freely under gravity. In order to increase the powder packing density after depositing the powders on the substrate, a rigid plane is used to compress the powder bed to simulate the pressure implemented by the recoater blade and pressing plate during experiments.

<Insert Figure 2>

To achieve the powder deposition for multiple materials, the powder-generating plane is divided into small sections and the generation rate of each specific powder material on each section is adjusted to meet the required deposition pattern. Fig. 3 shows the simulated powder bed results using powder deposition patterns employed in previous multi-material SLM studies. Fig. 3(a) presents the distribution of evenly mixed Cu10Sn and 316L powders, which can be used to create easy-to-remove composite material for support structures [10]. Fig. 3(b) and Fig. 3(c) show a clear boundary between Cu10Sn and 316L powders, where Fig. 3(c) illustrates the 'finger-cross' shaped interfacial design which can help enhance the elemental diffusion between the two materials [11]. Fig. 3(d) presents a gradient powder distribution pattern for manufacturing functionally graded components [13], which is obtained by gradually decreasing the generation rate of Cu10Sn powder from 100% to 0% from left to right, while inversely increasing the generation rate of 316L powder from 0% to 100%.

<Insert Figure 3>

By employing this multi-material powder deposition method, various combination of powder materials can be deposited on the same building layer and across different layers with required deposition patterns, providing great flexibility for different multi-material additive manufacturing systems.

2.3 Modelling of laser-powder interaction

After depositing the powder layer, the calculated powder information is transferred to a CFD model to simulate the interaction between the laser beam and powders. The following

assumptions were introduced to help develop the continuum CFD model: (i) the fluid flow was assumed as a incompressible, Newtonian and laminar flow [38], (ii) the enthalpy-porosity technique introduced by Voller et al. [39] was adopted to simulate the material melting and solidification process, (iii) mass loss due to vaporization was not included in the model [38] and (iv) the Boussinesq approximation was formulated to account for the density change caused by temperature variation in the molten pool [22].

Based on these assumptions, the three-dimensional mass, momentum and energy conservation equations are represented in equations (5)-(7) [40, 41] as follows:

$$\frac{\partial \rho}{\partial t} + \nabla \cdot (\rho \vec{v}) = 0 \tag{5}$$

$$\frac{\partial}{\partial t}(\rho \vec{v}) + \nabla \cdot (\rho \vec{v} \vec{v}) = -\nabla p + \nabla \cdot (\bar{\bar{\tau}}) + \rho \vec{g} + S_{mom} \tag{6}$$

$$\frac{\partial(\rho H)}{\partial t} + \nabla \cdot (\rho \vec{v} H) = \nabla \cdot (k \nabla T) + S_h \tag{7}$$

where ρ is the material density, t is the time, $\vec{v}$ is the fluid velocity, p is the pressure, $\bar{\bar{\tau}}$ is the stress tensor, $\rho \vec{g}$ is the gravitational body force, H is the enthalpy, k is the thermal conductivity, S_{mom} is the momentum source and S_h is a self-adaptive volumetric heat source.

Fig.4 illustrates the boundary conditions of the calculation domain, where thermal conduction, convection and radiation are applied on the side and bottom surfaces of the substrate defined as walls. The energy-balance equation is expressed as shown in equation (8):

$$k \cdot \frac{\partial T}{\partial \boldsymbol{n}} = -h_c(T - T_{env}) - \sigma \varepsilon (T^4 - T_{env}^4) \tag{8}$$

where h_c is the heat convection coefficient, σ is the Boltzmann constant, ε is the radiation emissivity and T_{env} is the environmental temperature. The top and side surfaces of the gas phase are defined as a pressure outlet, open to the ambient atmosphere with zero gauge-pressure.

\<Insert Figure 4\>

Apart from the two powder materials 316L and Cu10Sn, a gas phase is included, so that the surface tension forces on the free surface between the gas and molten metal phases can be accurately captured. The volume of fluid (VOF) [42] method is employed to track the interface

7

between these three phases. The liquid-gas free surface between the gas phase and metal phases, as well as the interface between the two metal phases can be distinguished by comparing the volume fractions of these three phases during each time step. Other user-defined momentum and energy sources are also added to this liquid-gas interfacial boundary. The conservation equation for the volume fraction may be expressed as shown in equation (9) [43]:

$$\frac{\partial F}{\partial t} + \nabla \cdot (\vec{v}F) = 0 \qquad (9)$$

where F is denoted as the volume fraction of a certain phase. The characteristics of the molten pool evolve rapidly during SLM process, and thus the conservation of the applied heat source is necessary. If the heat source is applied arbitrarily on the free surface, the amount of total heat input from the laser beam will vary between two moments. Therefore, a self-adaptive Gaussian distributed laser beam is employed as a volumetric heat source on the free interface between the gas and metal to meet the conservation of total heat input for the changing molten pool profiles. Assuming that a total number of n cells are located on the interface within the effective laser beam range, heat source S_h can be expressed as shown in equation (10):

$$S_h = \frac{P_{laser}*\eta}{V_{cell}*\Sigma_1^n \exp\left(-\frac{N*r_n^2}{r^2}\right)} * \exp\left(-\frac{N*r_n^2}{r^2}\right) \qquad (10)$$

where V_{cell} is the cell volume, P_{laser} is laser power, η is the laser power absorptivity. N is the Gaussian coefficient which is related to the percentage of laser power concentrated within the laser beam radius [44]. In this study, 95% of the total power was assumed to be contained within the laser beam radius r [45], and hence $N = 3$ was applied as the Gaussian coefficient. r_n is the radial distance from the laser beam centre which is given as equation (11):

$$r_n = \sqrt{\left[y_n - (v_{laser}*t_{flow} + y_0)\right]^2 + (x_n - x_0)^2} \qquad (11)$$

where v_{laser} is the laser scanning speed, t_{flow} is the calculation flowing time, x_0 and y_0 define the x and y positions of the starting point on the powder bed. Laser beam absorptivity η is difficult to measure experimentally because it is dependent on many factors including laser wavelength, surface roughness, material of the substrate and process parameters (laser power, laser incident angle and laser spot size etc.) [16, 46]. The laser beam absorptivity of 316L was adopted as 0.35 in this model, which was a decision informed by previous studies of Khairallah et al. [14, 16]. Compared to iron-based alloys, the laser absorptivity of copper alloy was much lower and would decrease rapidly with the increase of laser wavelength. Since a continuous

8

fibre laser was used during the process, at 1070 nm wavelength the laser beam absorptivity of copper was 0.03 [47, 48]. Due to the lack of reliable material parameters for Cu10Sn, the laser beam absorptivity of Cu10Sn was also treated as 0.03 in this study.

The recoil pressure P_r acts normal to the local free surface which is calculated as a function of the liquid surface temperature defined as [49]:

$$P_r = 0.54P_0 exp\left(\Delta H_{vap}\frac{T-T_{vap}}{RTT_{vap}}\right) \tag{12}$$

where P_0 is the atmospheric pressure, T_{vap} is the vaporization temperature, ΔH_{vap} is the enthalpy of vaporization and R is the universal constant of gases.

Surface tension plays an important role in the development of the molten pool during SLM processes. The continuum surface force (CSF) model [50] is used to calculate the surface tension which is added as a source term to the momentum equation. Two surface-tension forces are included in this model: (1) surface-tension force, f_{sn}, normal to the free surface generated as a result of the curvature developed by the interface between the metal and gas phase and (2) the Marangoni shear force, f_{st}, tangential to the free surface generated as a result of surface-tension difference attributed to the temperature difference on the molten pool surface. The surface tension forces can be defined as shown in equation (13) [51] :

$$f_S = f_{sn} + f_{st} = \sigma \cdot \kappa \cdot \vec{n} + \nabla_t \sigma \tag{13}$$

where σ is surface tension, κ is surface curvature and $\vec{n}$ is the vector normal to the surface.

Buoyancy force is considered using Boussinesq approximation [52], expressed as given in equation (14):

$$S_{buoyancy} = (\rho - \rho_m)g \approx -\rho_m\beta(T - T_m)g \tag{14}$$

where ρ_m is the material density at melting temperature T_m and β is the thermal expansion coefficient. An approximation is made, where $\rho = \rho_m(1 - \beta\Delta T)$, in order to eliminate the variance of material density which is dependent on the temperature.

For the implementation of the CFD model, ANSYS Fluent v18.2 is used to solve all the transport equations. A three-dimensional model is built and a pressure-based transient solver with PISO (Pressure-Implicit with Splitting of Operators) pressure-velocity coupling method is applied. The velocity and temperature fields are discretized with a second order upwind scheme, and the pressure field is discretized with a PRESTO! (PREssure STaggering Option)

scheme which is applicable for the VOF method. The convergence criteria for residuals of continuity and momentum equation are satisfied by applying default value as 10^{-3} and 10^{-6} for the energy equation. The dimensions of the calculation domain were 500 μm $\times$720 μm $\times$ 240 μm, which contained 691,200 hexahedral cells with uniform grid spacing of 5 μm. The calculation time step was 1×10^{-6} s with courant number kept smaller than 1. Table 1 presents the thermal properties of 316L and Cu10Sn powders used in this study [12, 23, 53, 54, 55]. Due to the limitation of existing experimental data, the properties of Cu10Sn were regarded as constant values not subjected to the temperature change.

<Insert Table 1>

3. Results and discussions

3.1 Multi-track simulation

Before introducing Cu10Sn into the model, process parameters were varied to investigate the impact of energy input on the molten pool development and track formation during multi-track and multi-layer SLM process using 316L as powder material. A laser power of 100 W and a scanning velocity of 800 mm/s along positive Y direction were initially employed to carry out the simulation, before incrementally increasing the laser power. For these simulations the laser spot size was set at 70 μm, and the heating duration of the first single track was set as 648 μs with a total scanning length of 518 μm. After scanning the first track, the laser scanning direction was altered 90° towards positive X, and the laser travelled for 36 μs to achieve a hatch spacing of 28.8 μm. Thereafter an adjacent track was scanned in parallel with the first track along negative Y direction. A schematic of the scanning path is shown in Fig. 5. After removing the laser heat source, 200 μs of cooling time was applied to account for the solidification process of the molten material.

<Insert Figure 5>

Fig. 6 and Fig. 7 present the results of simulations for various applied laser powers, ranging from 100 W to 200W. Fig. 6 shows the molten pool morphology, while Fig. 7 presents a cross-section of the molten pool at different stages of the scanning process. Fig. 8 shows the temperature and molten pool velocity fields for higher laser powers, 175 W and 200 W.

<Insert Figure 6>

<Insert Figure 7>

Fig. 6(a) presents the temperature field and molten pool morphology using 100 W laser power at 324 µs, in the middle of the first scanning track, while Fig. 6(b) shows the molten pool characteristics when changing the scanning direction. It can be observed that a discontinuous bead was obtained after the first track and most of the powders on the scanning path were only partially melted with limited fusion formed among the powders. After scanning the second track more powders were melted as seen in Fig. 6(c). This could be attributed to the fact that the temperature of the surrounding powders increased after the first scanning track as a result of heat conduction, and during the scanning of the second track some portion of the solidified bead was re-melted. Fig. 7(a) shows the molten pool status when the laser was passing the middle of the powder bed along the plane of the laser beam centre, while Fig. 7(b) presents the cross-section of the track when the laser was approaching the end of the first scanning track. Balling effect can be observed with isolated clusters distributed on the substrate. This is consistent with the study by Li et al. [56], which reported that when a low laser energy density was applied, the balling phenomenon could occur due to the poor wetting characteristic of the molten pool, leading to the discontinuity of the bead after solidification. Comparing the highlighted regions in Fig. 7(a) and (b), before and after the laser beam interacted with the powder, it can be noted that the individual powder particles bonded with neighbouring particles as small droplets during melting, as a result of surface tension, which then formed separate balls after solidification.

When the laser power was increased to 150 W, as shown in Fig. 6(d)-(f), the balling phenomenon disappeared, and a better surface finish was achieved, along with continuous bead.

However, some waviness can still be observed on the track surface, as shown in Fig. 7(d). This finding can be further supported by the theory of Plateau–Rayleigh instability [57], which describes the breaking of a long cylindrical fluid jet into droplets or short segments to minimise the surface energy. In both Fig. 6 and Fig. 7 the molten pool region is illustrated in red, with temperature higher than the melting point 1723 K, and there is a notable increase in molten pool size when using a laser power of 150W, compared to when using 100 W.

When increasing the laser power to 175 W, as illustrated in Fig. 6(g)-(i), a smooth track surface was obtained, with more elongated molten pool. Surface tension arises as a result of different attractive forces among molecules on the liquid free surface, and surface tension always has the tendency to minimise the area of the liquid surface. With a laser power of 175 W, the applied energy density was sufficient to melt a larger volume of powder and form a stable molten pool. The nearby molten particles were constantly pulled towards the molten pool due to surface tension, and thus contributing to a continuous bead without breakage. Marangoni stress induced flow is another important factor inside the molten pool which is mainly driven by the surface tension difference caused by temperature difference on the molten pool surface, leading to a phenomenon that the fluid will flow from low surface tension area to high surface tension area. Since surface tension-temperature coefficient was assumed to be negative throughout this study, an outward flow would form driving the liquid metal move from centre to the edge of the molten pool. When applied with 175 W laser power, a maximum velocity of 1.16 m/s was obtained inside the molten pool with an outward pattern bringing the liquid to the cooler area, as illustrated in Fig. 8(a).

When further increasing the laser power to 200 W a depression region appeared in the molten pool front, which could be attributed to the formation of keyholes, as shown in Fig. 6(j)-(l). When the temperature of the molten material exceeded the boiling point, the recoil pressure which was caused by the rapid vaporization of the liquid metal would apply an exponentially increased force normal to the local liquid surface. The evaporation temperature of 316L is 3090 K and the latent heat of vaporization is 7.45×10^6 J·kg^{-1}[23]. The resultant molten pool velocity near the keyhole region would increase dramatically due to the extra momentum imposed from the recoil pressure towards the free surface. Fig. 8(c) shows the molten pool morphology and velocity field when 200 W was applied, indicating 6.92 m/s maximum velocity inside the keyhole which was much higher than the velocity field in Fig. 8(a) without the keyhole formation. The balance among the recoil pressure, surface tension forces and hydrostatic liquid pressure would determine the development of the molten pool.

Keyhole formation during SLM was also investigated by Wu et al. [17]. They reported that after removing the heat source, without the impact of recoil pressure the liquid metal near the keyhole would start to fill the depression region and form a convex surface after solidification. Another study from Tang et al. [23] pointed out that a deep keyhole would appear when applied with high laser power, in which case combined with large powder layer thickness the keyhole depression would not fully close after solidification. Instead, near-spherical porosities might occur as a result of entrapped gas phase and the collapse of deep keyhole. In the current study of the first scanning layer, since the keyhole depression was not deep and the powder layer did not contain sufficient gas phase, the keyhole depression was recovered, and a convex track profile was formed after solidification. By comparing the molten pool characteristics of different laser powers presented in Fig. 7, it can be noticed that with low energy input (100 W), the energy was only enough to melt limited number of particles without reaching the substrate, and balling effect would occur to minimise the surface energy. With increased energy input, more powders were melted, and enough heat was transferred towards the substrate to melt the substrate, allowing the molten powder to be fully absorbed by the molten pool, therefore contributing to a continuous track surface.

<Insert Figure 8>

Fig. 7(i) shows the cross-section taken when the laser was approaching the middle of the second track with 200 W laser power, and Fig. 7(j) presents the molten pool status at the end of this track. The depth of the keyhole depression was noticably deeper in Fig. 7(i) compared to both the other moments of the first track shown in Fig. 7(g) and Fig. 7 (h) and the end of the second track shown in Fig. 7(j), given that the same laser power condition was applied. The maximum velocity inside the keyhole also increased from 6.92 m/s to 9.92 m/s at the same adjacent location of the first and second scanning track shown in Fig. 8(c) and (d), respectively.

<Insert Figure 9>

The development history of molten pool volume (Fig. 9) was extracted from the model to help explain the phenomenon. During the first track, the molten pool volume increased at the beginning before reaching a stable state, and this stable state continued until the laser beam finished changing the scanning direction at 684 µs. A significant increase in molten pool volume occurred at the beginning of the second track before reaching a maximum value, after which the molten pool volume started to decrease gradually. The cooling process began at 1332 µs when the heat sourse was removed from the model, and it took the longest for the molten pool to fully soildify when using 200 W laser power, due to the highest molten pool volume. The rapid volume increase at the beginning of the second track could be related to the fact that the adjacent region, which was overlapped by the second track, was recently melted by the laser beam, and hence the temperature was still high. The later decrease in molten pool volume indicates that the laser beam had started to move to a region of lower temperature, which had undergone a longer period of cooling. This also explains the phenomenon that the deepest keyhole depression occured towards the middle of the second track when the molten pool volume was the highest, which was also discussed by Khairallah et al. [14]. They suggested that the energy density should be reduced upon changing the scanning direction along a track to avoid deep keyhole depression, which could lead to the formation of pores. Without keyhole formation, in the case of 175 W laser power, despite the fact that the volume of the molten pool increased during the second scanning track as a result of heat accumulation, little much variation was observed in the velocity field, with maximum velocities of 1.16 m/s and 1.2 m/s, as seen in Fig. 8(a) and (b). This could be attributed to the fact that, without the effect of recoil pressure, the flow was mainly driven by the Marangoni stress, and thus the molten pool dynamics were less influenced by the increase of temperature.

3.2 Multi-layer simulation

To allow the simulation of multiple layers, after cooling, the surface geometry of the solidified first layer was extracted from the model. The surface geometry which was the interface between the gas phase and metal phases was reconstructed using geometric reconstruction scheme during the calculation. After solidification, the isosurfaces of the volume fractions of the two metal phases were plotted and exported as STL file to DEM. Considering that the temperature had increased because of the heating process during the first layer, the temperature distribution of the solidified powder bed was also exported. DEM was then employed to deposit a second powder layer on the solidified profile, which now was regarded as the new substrate during the simulation. The sizes and positions of the newly deposited

powder particles were then transferred from DEM back into CFD to carry out the thermo-fluid calculation. During the initialization of the second layer simulation, volume fractions of the newly added powders, as well as the first layer, were assigned as 316L material. The temperature profile of the solidified first layer was used as an input to initialize the temperature distribution of the calculation domain. After the initialization of the phase and temperature field, two adjacent tracks were scanned with varying laser powers, again ranging from 100 W to 200 W for the second layer. The simulated temperature distribution and bead morphology are presented in Fig. 10, while cross-sections along the plane of the laser beam centre are shown in Fig. 11.

\<Insert Figure 10\>

Similar to the first layer, a discontinuous track with balling effect was observed when applying 100 W laser power, as seen in Fig. 10(a)-(c). Due to insufficient heat input, only the surface exposed to the laser beam was melted, and separate clusters were formed to reduce the surface energy. Since insufficient heat was transferred to re-melt the first solidified layer, the interlayer fusion between the two layers was poor, and a severe lack of fusion could be observed, as shown in Fig. 11(a) and (b). A further interesting finding was that the balling effect also occurred in the second layer when 150 W laser power was applied (shown in Fig. 10(d)-(f)), despite the fact that a continuous bead was obtained when the first layer was processed (Fig. 6(d)-(f)). Yan et al. [27] stated that the balling effect could be attributed to the lack of melting of the substrate underneath the powder. In this case, even though the first solidified layer provided some heat to help form a larger molten pool, the balling effect still happened. The surface roughness of the previously solidified layer was also found to be an important factor in influencing the thickness of the new powder layer, which would determine the wettability of the molten pool [23], and hence affect the balling effect and porosity formation.

\<Insert Figure 11\>

As previously discussed, some waviness was observed on the track of the first layer, when using 150 W laser power (Fig. 7(d)). This could introduce more gas phase in between the powder particles when a new powder layer was deposited. In comparison with the solid substrate, the effective thermal conductivity of loose powder is much lower, due to the low thermal conductivity of the gas phase [58, 59]. As a result, heat cannot be transferred to the solidified layer and the underlying substrate quickly enough without sufficient heat input, which can add to the fluctuations of the molten pool. Such instability contributes to the formation of a disconnected balling effect, as demonstrated in Fig. 11(c) and (d). When increasing the laser power to 175 W and 200 W, the breakage of the long molten pool disappeared (shown in Fig. 10(i) and (l)) towards the end of the second scanning track. A significant increase of molten pool volume was observed during the second layer of scanning. Marangoni stress induced flow, as well as recoil pressure, would drive the liquid metal to the rear region of the long molten pool, resulting in a sloped molten pool front, as shown in Fig. 11(e)-(h).

3.3 Multi-material simulation

For multi-material simulation, the Cu10Sn phase was introduced, and Cu10Sn powders were deposited on the scanned track to form a second powder layer. Fig. 12(a) presents the morphology of the first scanned track of 316L (as previously shown in Fig. 6(i)), and Fig. 12(b) shows the morphology with a second layer of Cu10Sn powder applied. 175 W laser power and 800 mm/s scanning velocity were first employed to examine the evolution of the molten pool characteristics when the same energy density was applied to materials with different thermal properties. The resultant temperature field of the powder bed at the end of the first track is shown in Fig. 12(c).

<Insert Figure 12>

Only limited fusion was formed among the Cu10Sn powders, and a much lower temperature distribution field was obtained on the powder bed compared to when a second layer of 316L was applied (Fig. 10(h)). Since the cooling interval after the first scanned layer was set to be 200 μs, the temperature of the powder bed along the scanning centreline was still higher than the melting point of Cu10Sn when depositing the second Cu10Sn powder layer on top of 316L.

16

Despite this, a continuous melting of the Cu10Sn powders was not obtained. As mentioned in Section 2.3, the laser absorptivity of Cu10Sn was adopted as 0.03 in this study, which was less than 10% of the laser beam absorptivity of 316L. Furthermore, the thermal conductivity of Cu10Sn powder is higher than that of 316L, meaning that the heat is dissipated more efficiently by Cu10Sn from the laser beam centre towards the surrounding powders. The combination of these two factors meant that the actual energy absorbed and retained by Cu10Sn powders was insufficient to develop a molten pool to melt the powder.

<Insert Figure 13>

A further comparative study was made by initializing the first powder layer with half 316L and half Cu10Sn powder, with a clear interface deposited on the same building layer, as illustrated in Fig. 13(a). Again, process parameters of 175 W laser power and 800 mm/s scanning velocity were employed, with laser scanning on the interface of the two powder materials. The morphology of the scanned track after solidification is shown in Fig. 13(c). Compared to Fig. 12(c), despite not having the effect of preheating from the previous scanned layer, a higher temperature field was achieved with both the 316L and Cu10Sn powders being melted, as seen in Fig. 13(b). However, the size of region with temperature greater than 1723 K decreased significantly compared to when all of the powder was initialised as 316L (Fig. 6(h)). Fig. 14(a) and (b) present the temperature distribution at the middle and end moments of the scanning track. It can be seen that the temperature profile is not symmetric along the centreline: higher temperatures are shifted towards the 316L side around the molten pool region, while the Cu10Sn side exhibits slightly higher temperatures in the peripheral area further away from the centreline. Such asymmetric temperature distribution is found comparable to what was reported in dissimilar laser welding of copper to stainless steel, where a higher temperature field was obtained on the stainless side inside the fusion zone [37, 60].

<Insert Figure 14>

Six measurement points were allocated on the substrate surface to examine the temperature development history of the process, with three on each side, symmetric to the centreline, as shown in Fig. 14(a). Comparisons of the temperature development histories are presented in Fig. 14 (c-f). For the points located near the centreline (P1 and P4), the temperature on the 316L side increased faster than Cu10Sn, once the heat affected zone imposed by the moving laser beam reached the measurement points. This can be attributed to the fact that 316L has a poorer thermal diffusivity when compared to Cu10Sn. Since the heat could not be dissipated quickly by 316L, a higher maximum temperature was achieved for 316L (shown in Fig. 14(c)). Consequently, the maximum temperature region shifted towards the 316L side, contributing to the asymmetric temperature distribution on the powder surface near the centreline. For points P2 and P5, which were 50 µm away from the centreline, a lower temperature was obtained on the 316L side before the laser beam travelled to the plane, indicating that the heat dissipated from the laser beam centre would reach P5 earlier than P2. However, a rapid temperature increase was achieved on the 316L side when the laser beam centre arrived at this plane, after which the temperature of 316L exceeded that of Cu10Sn, as shown in Fig. 14(d). For points P3 and P6, which were far away from the centreline, Cu10Sn exhibited higher temperature field from the beginning, compared to 316L (seen in Fig. 14(e)). The combined temperature history of these six points is presented in Fig. 14(f), and it can be seen that the temperature difference between the points becomes less distinct as the laser beam moves towards the end of the scanning track.

The development histories of the molten pool volume for both Cu10Sn and 316L were extracted from the model to help understand the molten pool evolution, and are presented in Fig. 15. Despite the fact that the temperature field was higher on the 316L side near the centreline, more Cu10Sn particles were melted as a result of its lower melting point. It has been noted in Fig. 12(c) that the direct energy obtained from the laser beam failed to develop a continuous molten pool to melt the Cu10Sn powders when the powder bed was fully covered with Cu10Sn. It can also be observed from Fig. 15 that fewer Cu10Sn particles were melted at the beginning of the process, before 50 µs. Since 316L could retain more heat due to its low thermal conductivity, the molten pool was firstly formed on the 316L side. As a result of convection flow induced by Marangoni stress, the liquid 316L would flow from the centre towards the edge of the molten pool, bringing heat to the Cu10Sn side. Apart from the direct energy from the laser beam, the combination of heat conducted from the solid 316L powders and the heat brought by the convection flow from liquid 316L contributed to the melting of Cu10Sn powders.

<Insert Figure 15>

<Insert Figure 16>

In order to melt the powder bed fully covered with Cu10Sn powder, higher laser energy density was required to compensate for the low laser absorptivity and high thermal conductivity of Cu10Sn. As suggested by the work from Wei et al. [11], process parameters of 125 W laser power and 150 mm/s scanning speed were used to scan the second powder layer deposited with Cu10Sn, with the results of the simulation shown in Fig. 16. Fig. 16(a) presents the temperature distribution of the powder bed at the end of the first scanning track, while Fig. 16(b) shows the simulated result when approaching the end of the second track with 28.8 μm hatch spacing between two adjacent tracks. Interestingly, no distinct change was noticed on the track profile between the first and second track. When applied with the same hatch spacing for 316L, the track width was much more widened after scanning the second track compared to the first track (seen in Fig. 10(k) and (l)). This can be explained by the fact that during the first scanning track, more Cu10Sn particles close to the laser beam centreline would be melted and pulled towards the molten pool to form the track as a result of its low melting point and high heat conductivity. Consequently, with a small laser beam offset (hatch spacing) during the second track scanning, only limited number of particles around the laser beam centreline would be melted to increase the width of the scanning track. This was also reported by Wei et al. [11] where a greater hatch spacing was used for Cu10Sn during experiments. Fig. 16(c) presents the simulated track with an increased hatch spacing of 57.6 μm, and shows that a wider bead was obtained. The hatch spacing during real experiments could be further increased to improve the scanning efficiency considering that the effect of heat accumulation during multi-layer and multi-track process would be prominent. Fig. 16(d-f) show the comparison of track morphology after solidification for these three cases.

Fig. 17(a) presents a sandwich-layered component produced by a multi-material SLM system [11] which was developed in The University of Manchester. 175 W laser power and 800 mm/s scanning speed were employed to process the two 316L sections of 2 mm thickness, while an increased energy density of 125 W laser power and 150 mm/s scanning speed was used to fabricate the Cu10Sn sections of 1 mm thickness. Wire EDM was used to cut the sample

to get the cross-section, which was then ground and polished on a polishing machine. The interface between 316L layer and Cu10Sn layer was inspected using SEM and a clear boundary can be observed between the two materials, as shown in Fig. 17(b). It can be noted that some 316L phase has migrated into the newly processed Cu10Sn layer, which is also observed at the simulated interface, shown in Fig. 17(c).

<Insert Figure 17>

<Insert Figure 18>

Fig. 18 illustrates the development of molten pool cross-section at six moments, where the liquid fractions of 316L and Cu10Sn are represented in different colours. During the first scanning track, Cu10Sn powders were first melted when the laser beam impacted directly on Cu10Sn with lower melting point, shown in Fig. 18(a-c). Only limited melting occurred on the previously solidified 316L layer seen in Fig. 18(c) as a result of heat conduction. When processing the second scanning track, after offsetting the laser beam centre, the 316L substrate was more exposed to the laser beam, and thus 316L started to melt, as seen in Fig. 18(d). As a result of surface tension forces and buoyancy force, a convection flow formed inside the molten pool, mixing two materials with connected liquid channels, shown in Fig. 18(e). The rapid evolution of the molten pool contributed to the breakage of the 316L liquid channel into two separate sections, shown in Fig. 18(f). After solidification, some elements of 316L alloys appeared in the Cu10Sn layers near the interface resulting in a certain degree of elemental diffusion. This explains the phase migration observed in Fig. 17(b).

4. Conclusion

In this study, an integrated modelling framework has been developed to simulate multi-track, multi-layer and multi-material SLM processes. The molten pool development of multiple materials on the same building layer, and across different layers, were examined. The interface between two layers of different materials was visualised by simulation, and the formation of

phase migration at the interface was investigated. From the analysis of the modelling results and comparison with experiments, the following conclusions can be drawn:

- Despite a continuous track being obtained during the first scanning layer, balling effect could still happen in the second layer with the same applied energy. The poor surface roughness of the previously scanned track introduced more gas phase during the deposition of the second layer, which brought instability to the molten pool formation.

- The velocity field inside the molten pool and the depth of keyhole depression were related to the overall molten pool volume. As a result of heat accumulation, it is suggested that the energy density should be adjusted upon changing the scanning direction and across different layers to maintain a constant molten pool profile.

- Due to the different thermal properties of 316L and Cu10Sn, molten pool development would appear differently when the same energy input was applied. In order to melt the powder bed fully covered with Cu10Sn, higher laser energy density was required to compensate for the low laser absorptivity and high thermal conductivity. Greater hatch spacing should be adopted for Cu10Sn to obtain the best scanning efficiency.

- When the two powder materials were placed on the same building layer, the 316L powders melted first, and the heat conducted from the solid 316L powder, as well as the heat brought by the convection flow from liquid 316L, contributed to the melting of Cu10Sn powders. The phase migration at the interface was found to be related to the convection flow inside the molten pool, which contributed to the mixing of the two materials as well as elemental diffusion.

Attributed to the flexibility of this framework, various combination of powder materials for multi-material SLM can be explored prior to experiments, which provides valuable insights on the design and optimization for multi-material additive manufacturing systems. This modelling framework can be further expanded to a multi-scale model in future studies, which will incorporate the current temperature history analysis with microstructure evolution and local/global residual stresses development for multi-material SLM process.

Acknowledgements

Reference

[1]   J.P. Kruth, L. Froyen, J. Van Vaerenbergh, P. Mercelis, M. Rombouts, B. Lauwers, Selective laser melting of iron-based powder. Journal of Materials Processing Technology. (2004);149(1):616-22.

[2]   G.N. Levy, R. Schindel, J.P. Kruth, RAPID MANUFACTURING AND RAPID TOOLING WITH LAYER MANUFACTURING (LM) TECHNOLOGIES, STATE OF THE ART AND FUTURE PERSPECTIVES. CIRP Annals. (2003);52(2):589-609.

[3]   L. Thijs, F. Verhaeghe, T. Craeghs, J.V. Humbeeck, J.-P. Kruth, A study of the microstructural evolution during selective laser melting of Ti–6Al–4V. Acta Materialia. (2010);58(9):3303-12.

[4]   C.Y. Yap, C. Chua, Z. Dong, Z. Liu, D. Zhang, L.E. Loh, et al., Review of selective laser melting: Materials and applications. Applied Physics Reviews. (2015);2:041101.

[5]   Q. Han, Y. Gu, R. Setchi, F. Lacan, R. Johnston, S.L. Evans, et al., Additive manufacturing of high-strength crack-free Ni-based Hastelloy X superalloy. Additive Manufacturing. (2019);30:100919.

[6]   A.G. Demir, B. Previtali, Multi-material selective laser melting of Fe/Al-12Si components. Manufacturing Letters. (2017);11:8-11.

[7]   Z.H. Liu, D.Q. Zhang, S.L. Sing, C.K. Chua, L.E. Loh, Interfacial characterization of SLM parts in multi-material processing: Metallurgical diffusion between 316L stainless steel and C18400 copper alloy. Materials Characterization. (2014);94:116-25.

[8]   S.L. Sing, L.P. Lam, D.Q. Zhang, Z.H. Liu, C.K. Chua, Interfacial characterization of SLM parts in multi-material processing: Intermetallic phase formation between AlSi10Mg and C18400 copper alloy. Materials Characterization. (2015);107:220-7.

[9]   M. Zhang, Y. Yang, D. Wang, C. Song, J. Chen, Microstructure and mechanical properties of CuSn/18Ni300 bimetallic porous structures manufactured by selective laser melting. Materials & Design. (2019);165:107583.

[10]   C. Wei, Y.-H. Chueh, X. Zhang, Y. Huang, Q. Chen, L. Li, Easy-To-Remove composite support material and procedure in additive manufacturing of metallic components using multiple material laser-based powder bed fusion. Journal of Manufacturing Science and Engineering. (2019);141(7):071002.

[11]   C. Wei, L. Li, X. Zhang, Y.-H. Chueh, 3D printing of multiple metallic materials via modified selective laser melting. CIRP Annals. (2018);67(1):245-8.

[12]   C. Wei, Z. Sun, Y. Huang, L. Li, Embedding anti-counterfeiting features in metallic components via multiple material additive manufacturing. Additive Manufacturing. (2018);24:1-12.

[13]   C. Wei, Z. Sun, Q. Chen, Z. Liu, L. Li, Additive manufacturing of horizontal and 3D functionally graded 316L/Cu10Sn components via multiple material selective laser melting. Journal of Manufacturing Science and Engineering. (2019);141(8):081014.

[14]   S.A. Khairallah, A.T. Anderson, A. Rubenchik, W.E. King, Laser powder-bed fusion additive manufacturing: Physics of complex melt flow and formation mechanisms of pores, spatter, and denudation zones. Acta Materialia. (2016);108:36-45.

[15]   M.J. Matthews, G. Guss, S.A. Khairallah, A.M. Rubenchik, P.J. Depond, W.E. King, Denudation of metal powder layers in laser powder bed fusion processes. Acta Materialia. (2016);114:33-42.

[16]   S.A. Khairallah, A. Anderson, Mesoscopic simulation model of selective laser melting of stainless steel powder. Journal of Materials Processing Technology. (2014);214(11):2627-36.

[17]   Y.-C. Wu, C.-H. San, C.-H. Chang, H.-J. Lin, R. Marwan, S. Baba, et al., Numerical modeling of melt-pool behavior in selective laser melting with random powder distribution and experimental validation. Journal of Materials Processing Technology. (2018);254:72-8.

[18]   W. King, A.T. Anderson, R.M. Ferencz, N.E. Hodge, C. Kamath, S.A. Khairallah, Overview of modelling and simulation of metal powder bed fusion process at Lawrence Livermore National Laboratory. Materials Science and Technology. (2015);31(8):957-68.

[19] M. Zheng, L. Wei, J. Chen, Q. Zhang, C. Zhong, X. Lin, et al., A novel method for the molten pool and porosity formation modelling in selective laser melting. International Journal of Heat and Mass Transfer. (2019);140:1091-105.

[20] L.-X. Lu, N. Sridhar, Y.-W. Zhang, Phase field simulation of powder bed-based additive manufacturing. Acta Materialia. (2018);144:801-9.

[21] Y. Zhang, J. Zhang, Modeling of solidification microstructure evolution in laser powder bed fusion fabricated 316L stainless steel using combined computational fluid dynamics and cellular automata. Additive Manufacturing. (2019);28:750-65.

[22] C. Panwisawas, C. Qiu, M.J. Anderson, Y. Sovani, R.P. Turner, M.M. Attallah, et al., Mesoscale modelling of selective laser melting: Thermal fluid dynamics and microstructural evolution. Computational Materials Science. (2017);126:479-90.

[23] C. Tang, J.L. Tan, C.H. Wong, A numerical investigation on the physical mechanisms of single track defects in selective laser melting. International Journal of Heat and Mass Transfer. (2018);126:957-68.

[24] M. Bayat, S. Mohanty, J.H. Hattel, Multiphysics modelling of lack-of-fusion voids formation and evolution in IN718 made by multi-track/multi-layer L-PBF. International Journal of Heat and Mass Transfer. (2019);139:95-114.

[25] Z. Wang, W. Yan, W.K. Liu, M. Liu, Powder-scale multi-physics modeling of multi-layer multi-track selective laser melting with sharp interface capturing method. Computational Mechanics. (2019);63(4):649-61.

[26] S. Shrestha, S. Rauniyar, K. Chou, Thermo-Fluid Modeling of Selective Laser Melting: Single-Track Formation Incorporating Metallic Powder. Journal of Materials Engineering and Performance. (2019);28(2):611-9.

[27] W. Yan, W. Ge, Y. Qian, S. Lin, B. Zhou, W.K. Liu, et al., Multi-physics modeling of single/multiple-track defect mechanisms in electron beam selective melting. Acta Materialia. (2017);134:324-33.

[28] W. Yan, Y. Qian, W. Ge, S. Lin, W.K. Liu, F. Lin, et al., Meso-scale modeling of multiple-layer fabrication process in Selective Electron Beam Melting: Inter-layer/track voids formation. Materials & Design. (2018);141:210-9.

[29] A. Sorkin, J.L. Tan, C.H. Wong, Multi-material modelling for selective laser melting. Procedia Engineering. (2017);216:51-7.

[30] Q. Han, H. Gu, R. Setchi, Discrete element simulation of powder layer thickness in laser additive manufacturing. Powder Technology. (2019);352:91-102.

[31] R. Ganeriwala, T.I. Zohdi, A coupled discrete element-finite difference model of selective laser sintering. Granular Matter. (2016);18(2):21.

[32] Y.S. Lee, W. Zhang, Modeling of heat transfer, fluid flow and solidification microstructure of nickel-base superalloy fabricated by laser powder bed fusion. Additive Manufacturing. (2016);12:178-88.

[33] Y.S. Lee, P. Nandwana, W. Zhang, Dynamic simulation of powder packing structure for powder bed additive manufacturing. The International Journal of Advanced Manufacturing Technology. (2018);96(1):1507-20.

[34] EDEM 2019 User Guide: DEM Solutions Ltd., Edinburgh, Scotland, UK. Copyright ©; 2018.

[35] Surface energy and the contact of elastic solids. Proceedings of the Royal Society of London A Mathematical and Physical Sciences. (1971);324(1558):301.

[36] B.R. Moharana, S.K. Sahu, S.K. Sahoo, R. Bathe, Experimental investigation on mechanical and microstructural properties of AISI 304 to Cu joints by CO_2 laser. Engineering Science and Technology, an International Journal. (2016);19(2):684-90.

[37] A. Mannucci, I. Tomashchuk, V. Vignal, P. Sallamand, M. Duband, Parametric study of laser welding of copper to austenitic stainless steel. Procedia CIRP. (2018);74:450-5.

[38] L. Cao, Numerical simulation of the impact of laying powder on selective laser melting single-pass formation. International Journal of Heat and Mass Transfer. (2019);141:1036-48.

[39] V.R. Voller, A.D. Brent, C. Prakash, The modelling of heat, mass and solute transport in solidification systems. International Journal of Heat and Mass Transfer. (1989);32(9):1719-31.

[40] V.R. Voller, C. Prakash, A fixed grid numerical modelling methodology for convection-diffusion mushy region phase-change problems. International Journal of Heat and Mass Transfer. (1987);30(8):1709-19.

[41] G.K. Batchelor. An Introduction to Fluid Dynamics. Cambridge: Cambridge University Press; 2000.

[42] C.W. Hirt, B.D. Nichols, Volume of fluid (VOF) method for the dynamics of free boundaries. Journal of Computational Physics. (1981);39(1):201-25.

[43] M.H. Cho, Y.C. Lim, D.F. Farson, Simulation of weld pool dynamics in the stationary pulsed gas metal arc welding process and final weld shape. WELDING JOURNAL-NEW YORK-. (2006);85(12):271.

[44] W. Yan, W. Ge, J. Smith, S. Lin, O.L. Kafka, F. Lin, et al., Multi-scale modeling of electron beam melting of functionally graded materials. Acta Materialia. (2016);115:403-12.

[45] W.C. Tseng, J.N. Aoh, Simulation study on laser cladding on preplaced powder layer with a tailored laser heat source. Optics & Laser Technology. (2013);48:141-52.

[46] J. Trapp, A.M. Rubenchik, G. Guss, M.J. Matthews, In situ absorptivity measurements of metallic powders during laser powder-bed fusion additive manufacturing. Applied Materials Today. (2017);9:341-9.

[47] M. Naeem, Laser processing of reflective materials: a new technology managing reflection effects. Laser Technik Journal. (2013);10(1):18-20.

[48] S. Engler, R. Ramsayer, R. Poprawe, Process Studies on Laser Welding of Copper with Brilliant Green and Infrared Lasers. Physics Procedia. (2011);12:339-46.

[49] C. Jung-Ho, F.F. Dave, O.M. John, J.H. Kendall, Weld pool flows during initial stages of keyhole formation in laser welding. Journal of Physics D: Applied Physics. (2009);42(17):175502.

[50] J.U. Brackbill, D.B. Kothe, C. Zemach, A continuum method for modeling surface tension. Journal of Computational Physics. (1992);100(2):335-54.

[51] J.I. Arrizubieta, A. Lamikiz, F. Klocke, S. Martínez, K. Arntz, E. Ukar, Evaluation of the relevance of melt pool dynamics in Laser Material Deposition process modeling. International Journal of Heat and Mass Transfer. (2017);115:80-91.

[52] E.A. Spiegel, G. Veronis, On the Boussinesq Approximation for a Compressible Fluid. Astrophys J. (1960);131(2):442-7.

[53] K.C. Mills. Recommended values of thermophysical properties for selected commercial alloys: Woodhead Publishing; 2002.

[54] Y. Kawai, M. Kishimoti, H. Tsuru, Surface Tension and Density of Liquid Cu-Sn Alloys. J Japan Inst Metals. (1973);37(6):668-72.

[55] ECLIPSE COMBUSTION ENGINEERING GUIDE. 8th, editor. United States of America: Eclipse, Inc.; 1986.

[56] R. Li, J. Liu, Y. Shi, L. Wang, W. Jiang, Balling behavior of stainless steel and nickel powder during selective laser melting process. The International Journal of Advanced Manufacturing Technology. (2012);59(9):1025-35.

[57] V.G.e. Levich. Physicochemical hydrodynamics: Prentice Hall; 1962.

[58] D. Gu, P. Yuan, Thermal evolution behavior and fluid dynamics during laser additive manufacturing of Al-based nanocomposites: Underlying role of reinforcement weight fraction. Journal of Applied Physics. (2015);118(23):233109.

[59] Q. Han, H. Gu, S. Soe, R. Setchi, F. Lacan, J. Hill, Manufacturability of AlSi10Mg overhang structures fabricated by laser powder bed fusion. Materials & Design. (2018);160:1080-95.

[60] V.B. Shaibu, S.K. Sahoo, A. Kumar, Computational Modeling of Dissimilar Metal CO2 Laser Welding: Applied to Copper and 304 Stainless Steel. Procedia Engineering. (2015);127:208-14.
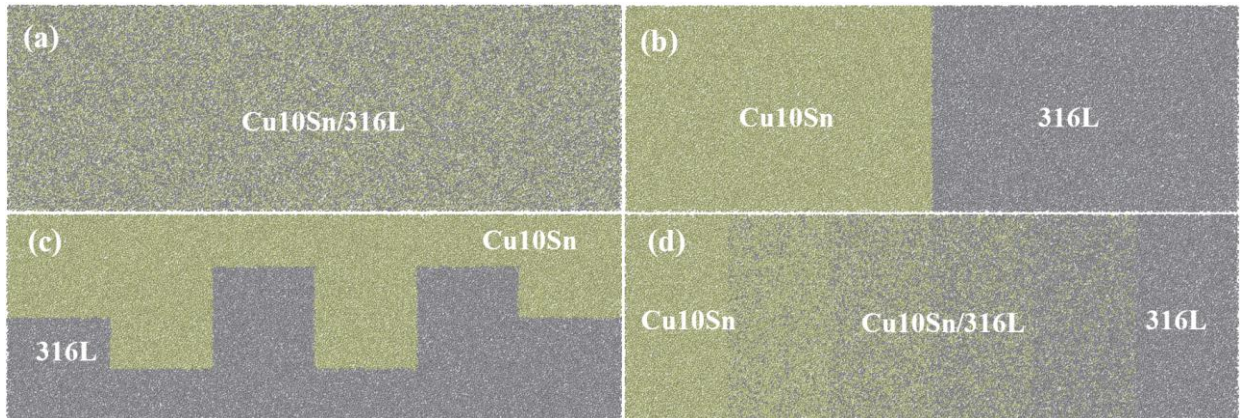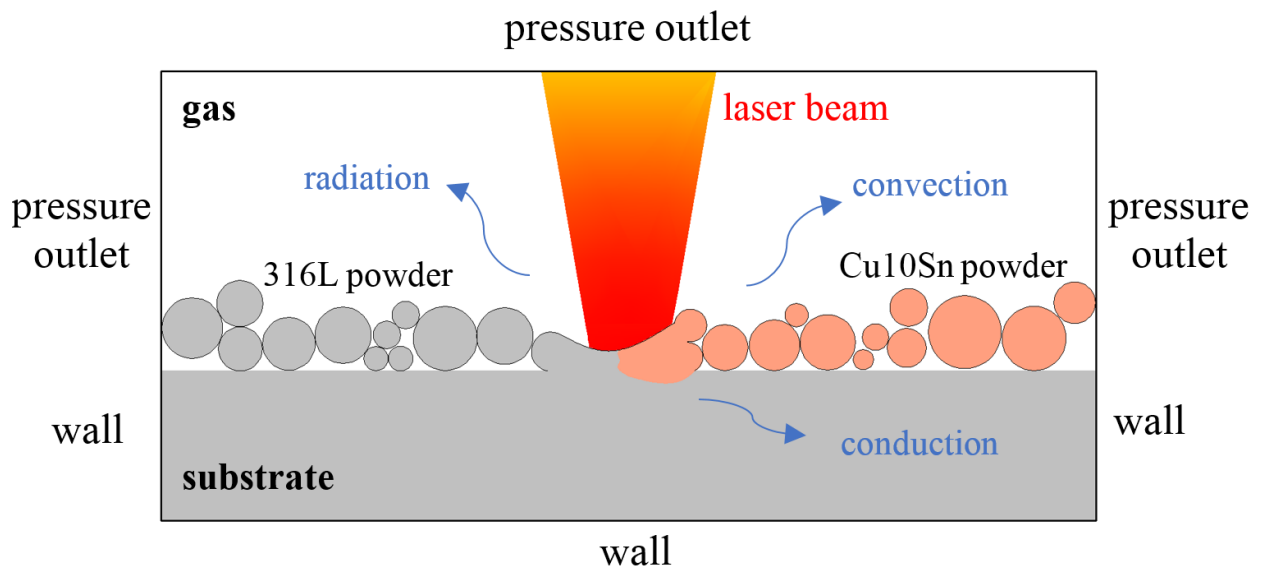
Figures
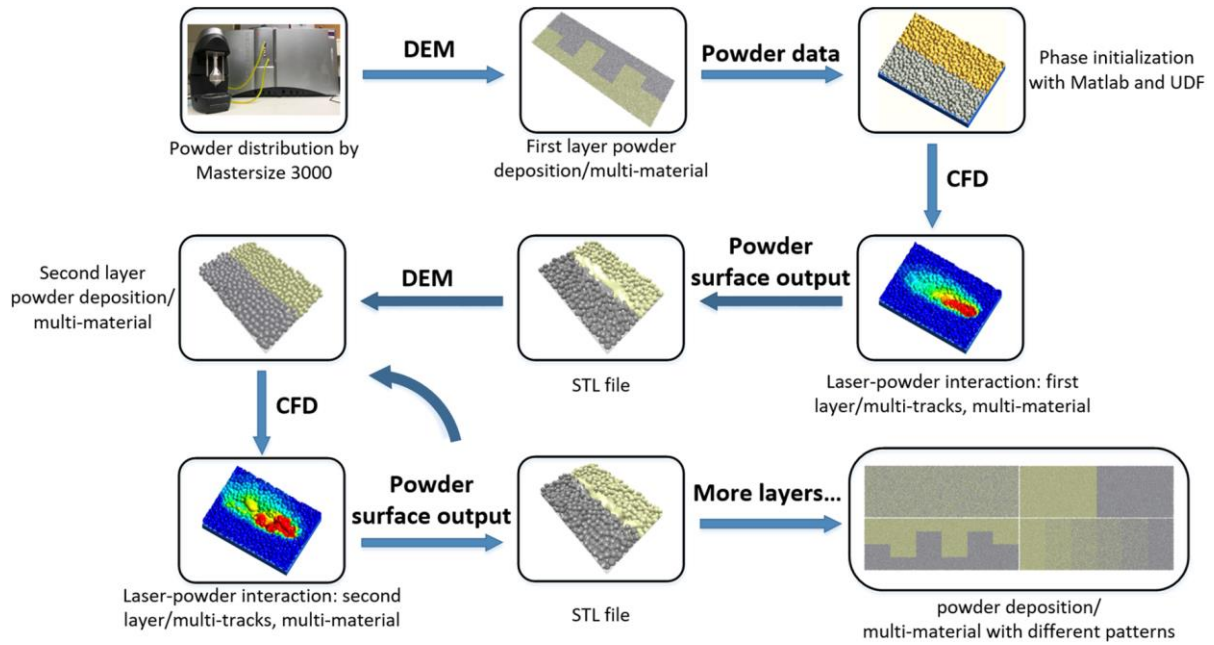
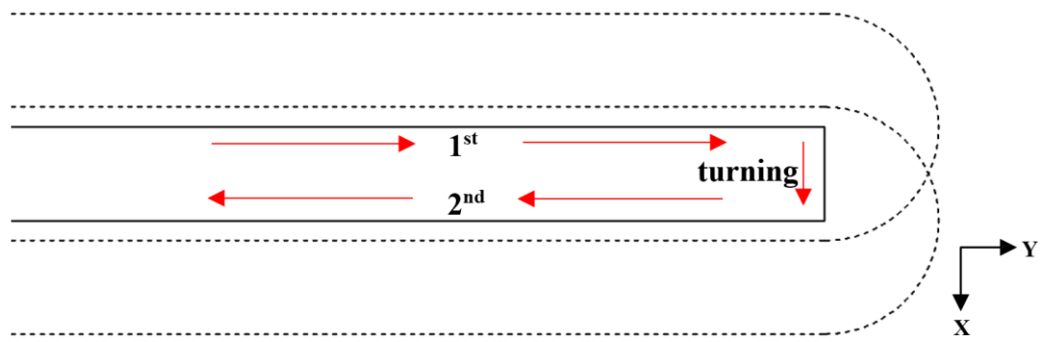**Fig. 1.** Framework for multi-track, multi-layer and multi-material SLM modelling
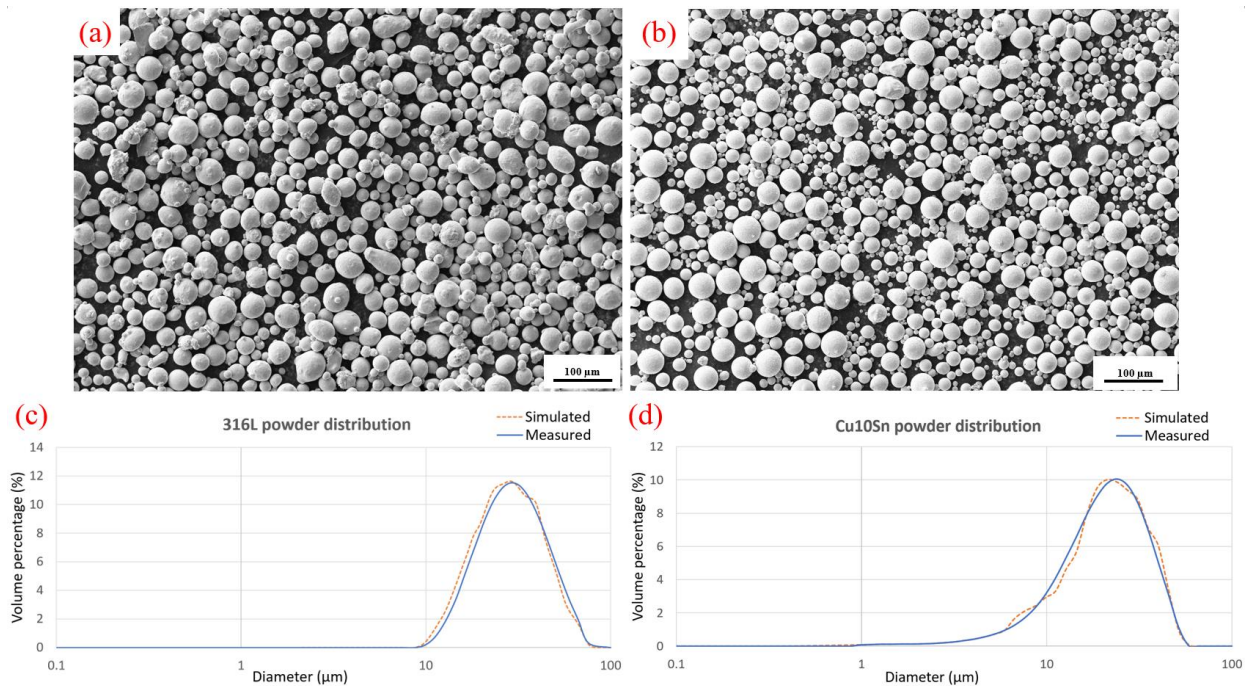
Fig. 3. Simulated powder deposition patterns for multi-material SLM process (a) evenly mixed, (b) clear boundary, (c) finger-cross shaped, (d) gradient
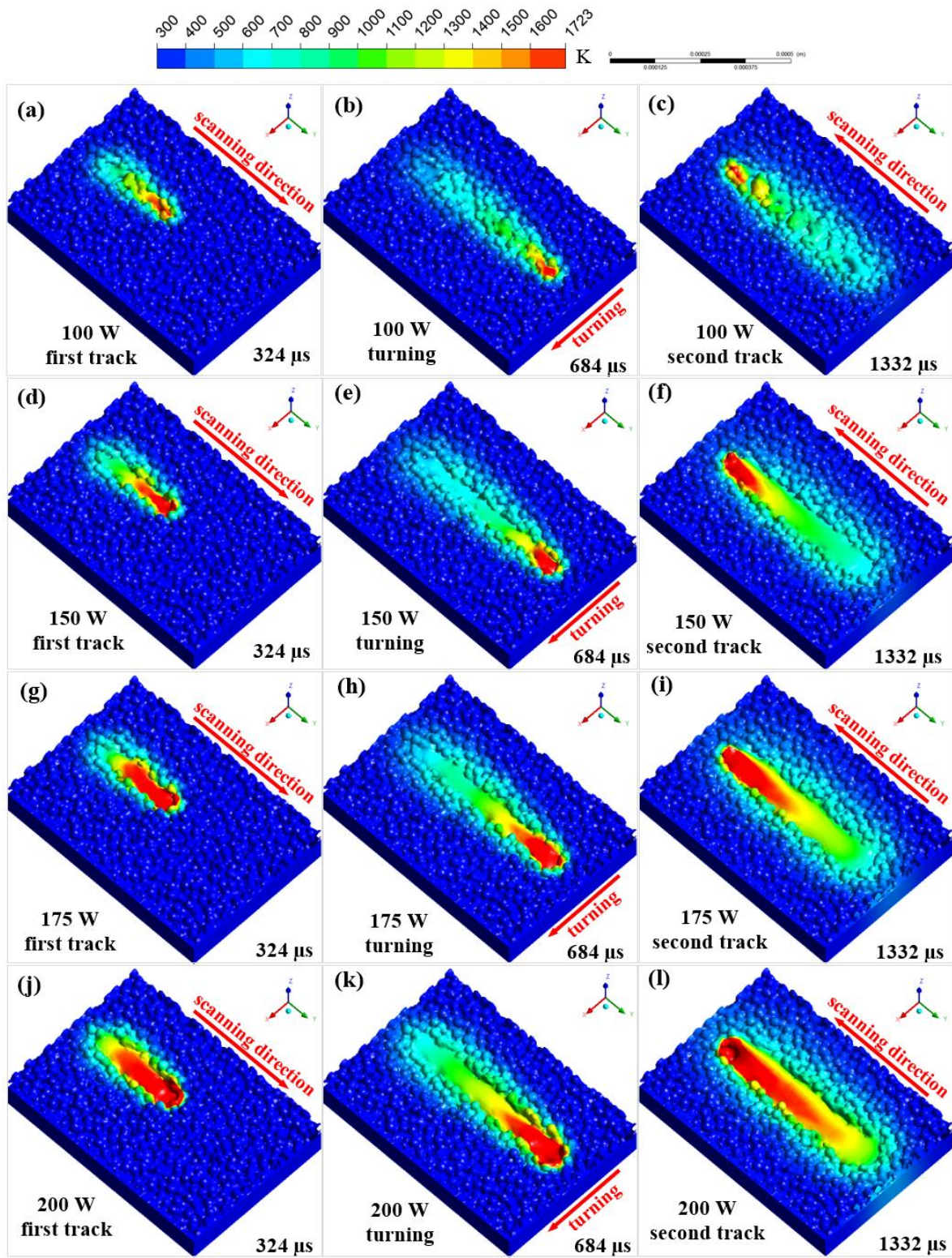

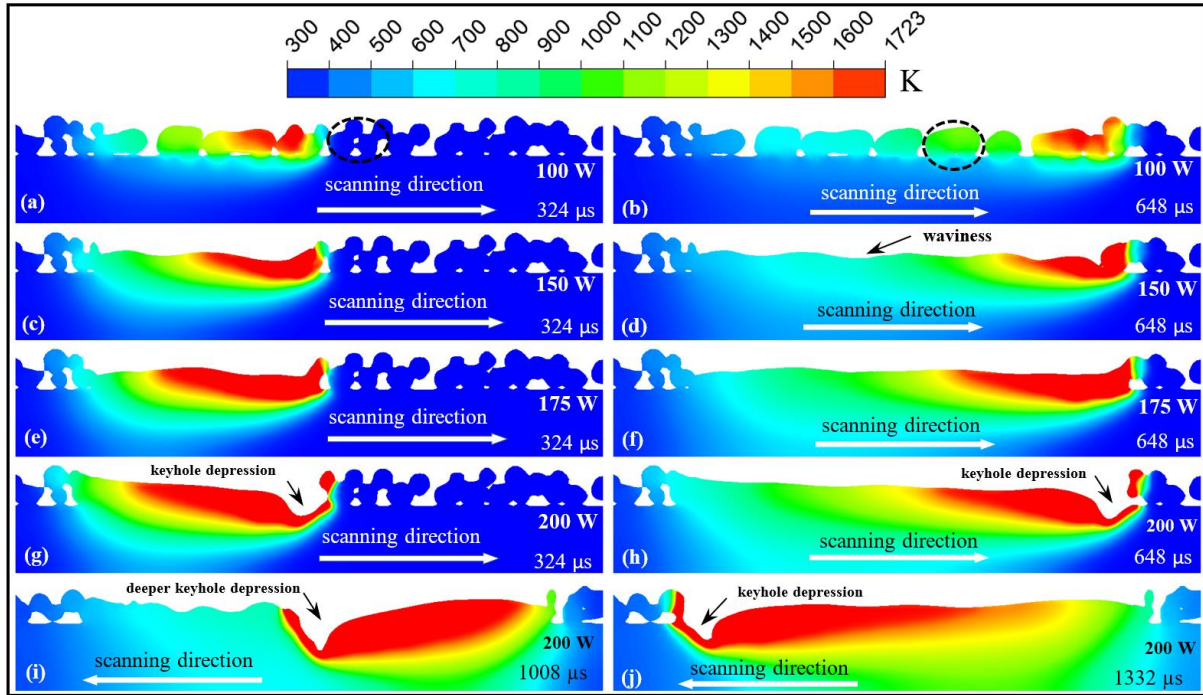**Fig. 4.** Thermal boundary conditions of the calculation domain

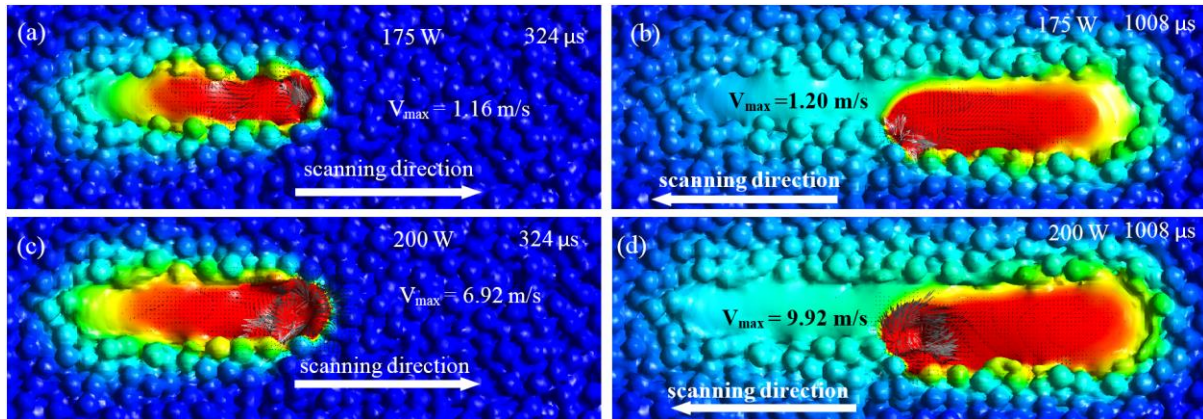**Fig. 5.** Schematics of the scanning pattern

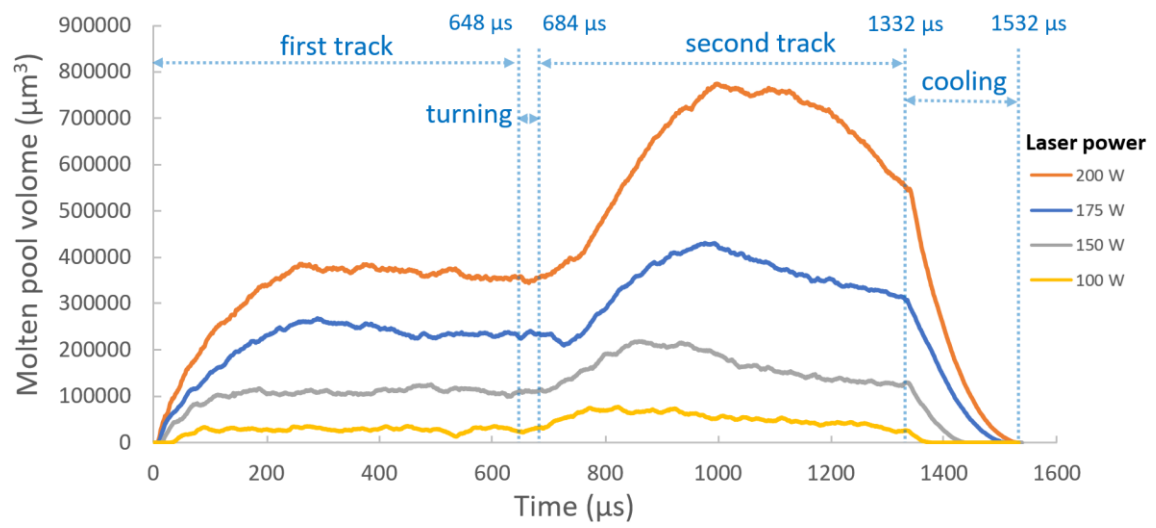**Fig. 6.** Temperature field and molten pool morphology of the first layer 316L with different laser powers at different moments

Fig. 7. Cross-section on the plane of laser beam center during the first layer of 316L, (a-h) X = 222 μm, (i-j) X = 250.8 μm

Fig. 8. Temperature and velocity field of 316L (a) 175 W first track at 324 μs, (b) 175 W second track at 1008 μs, (c) 200 W first track at 324 μs, (d) 200 W second track at 1008 μs

Fig. 9. Molten pool development history of the first layer 316L
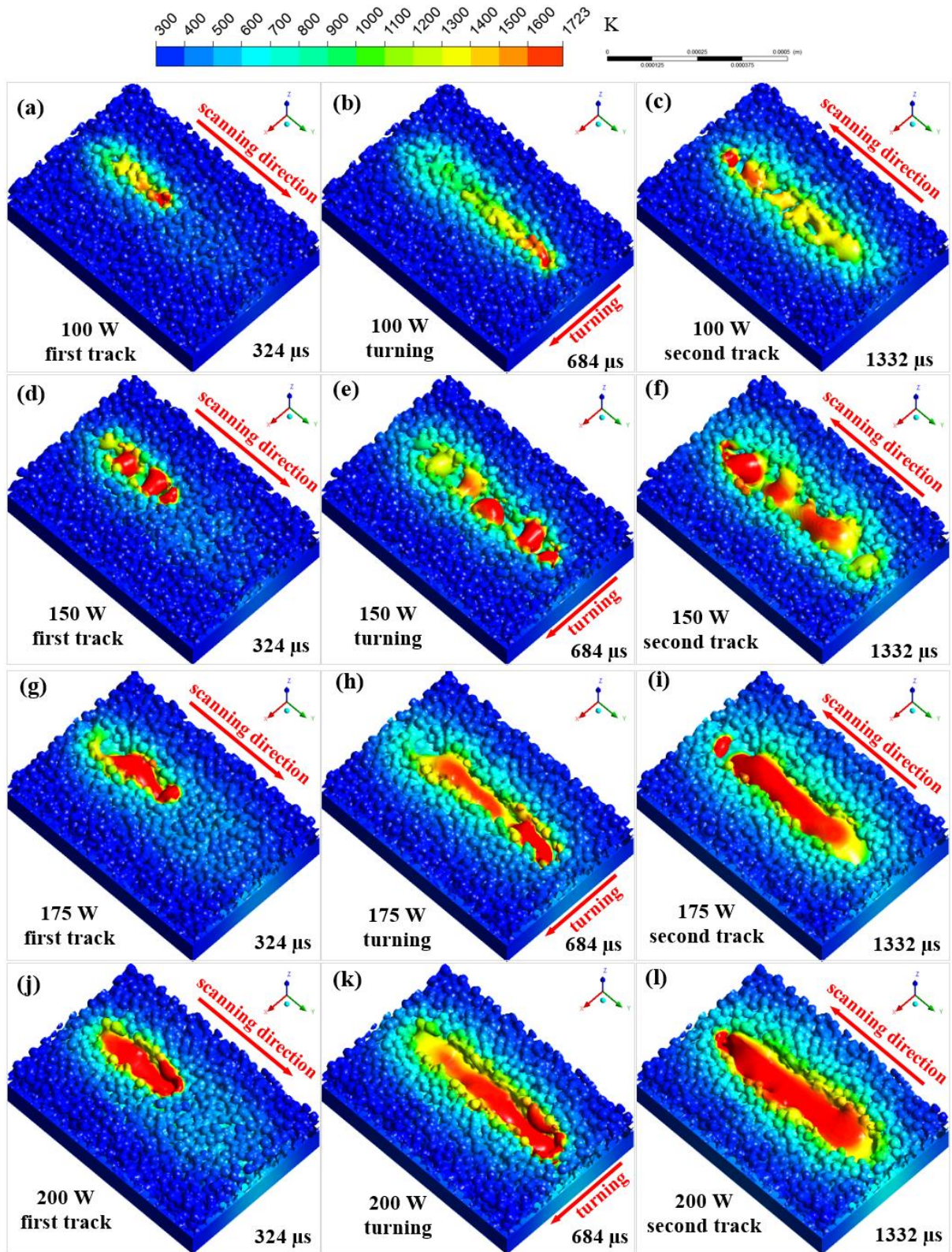
Fig. 10. Temperature field and molten pool morphology of second layer 316L with different laser powers at different moments
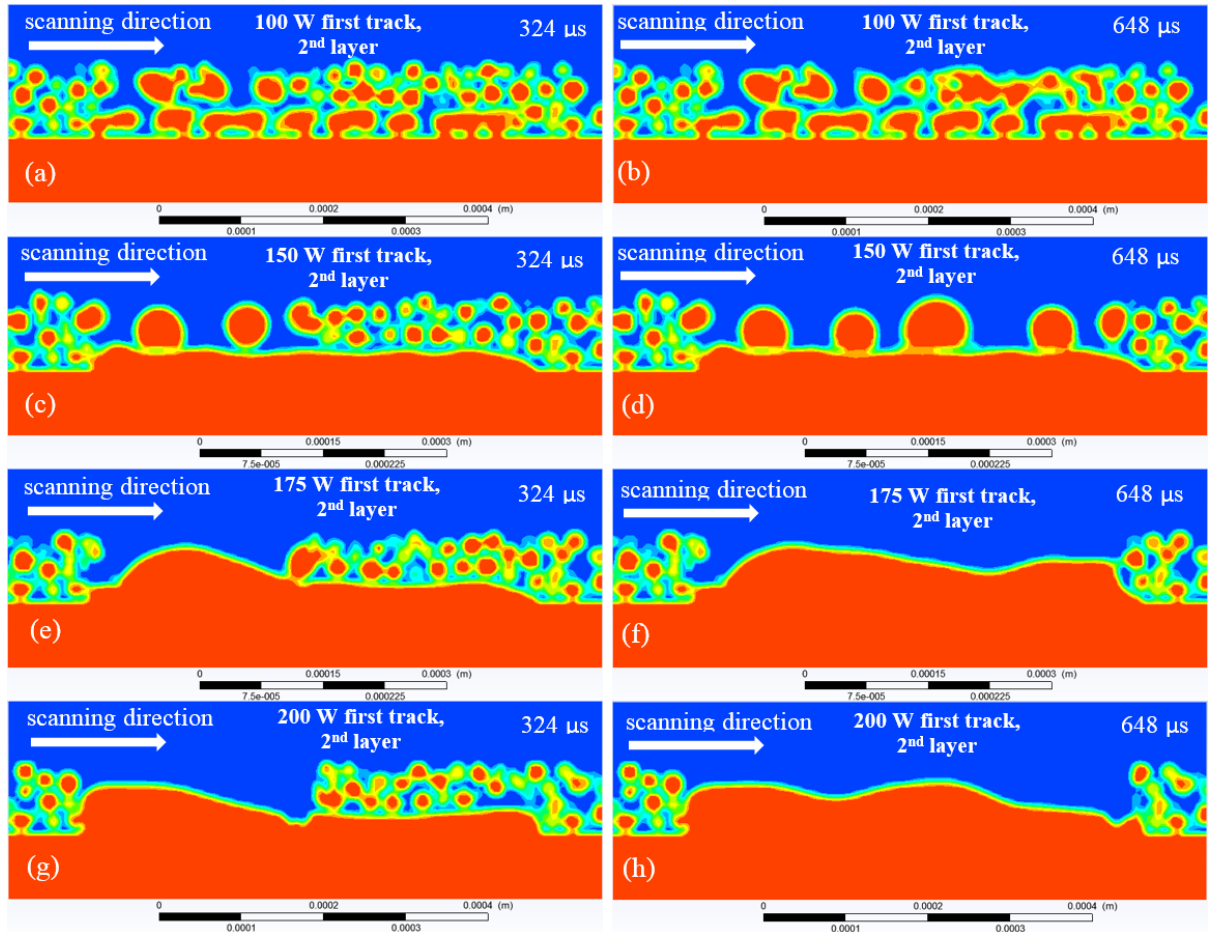
Fig. 11. Cross-section on the plane of laser beam centre during the second layer of 316L
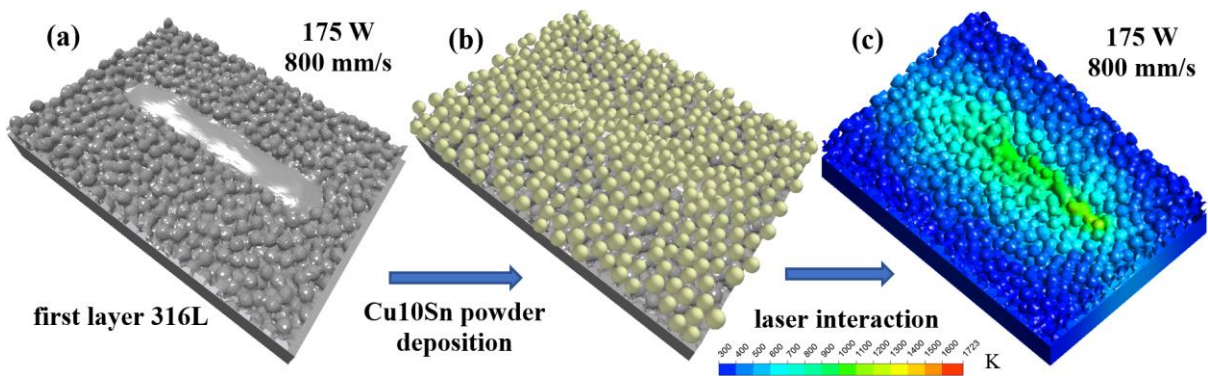
Fig. 12. (a) First layer 316L with 175 W and 800 mm/s, (b) second layer Cu10Sn powder deposition, (c) second layer Cu10Sn with 175 W and 800 mm/s
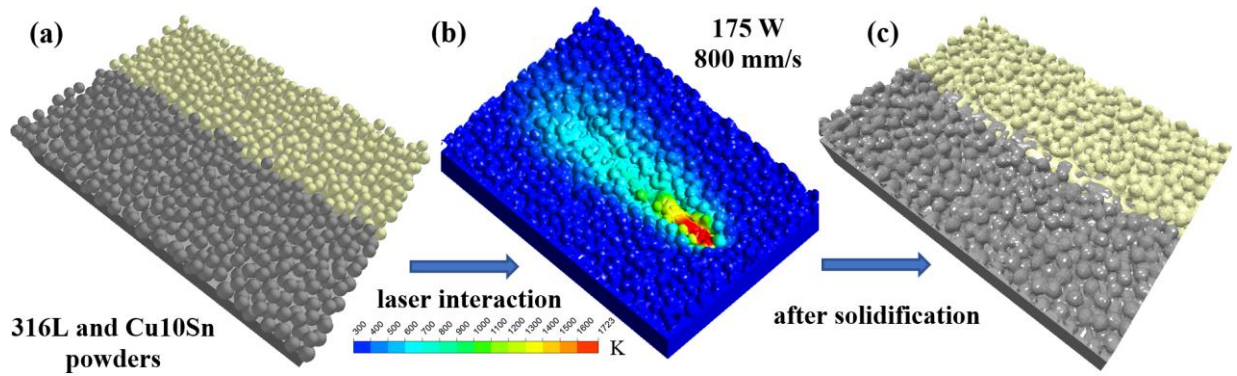
Fig. 13. (a) 316L and Cu10Sn powders with clear boundary, (b) laser beam applied on the boundary with 175 W and 800 mm/s, (c) track morphology after solidification
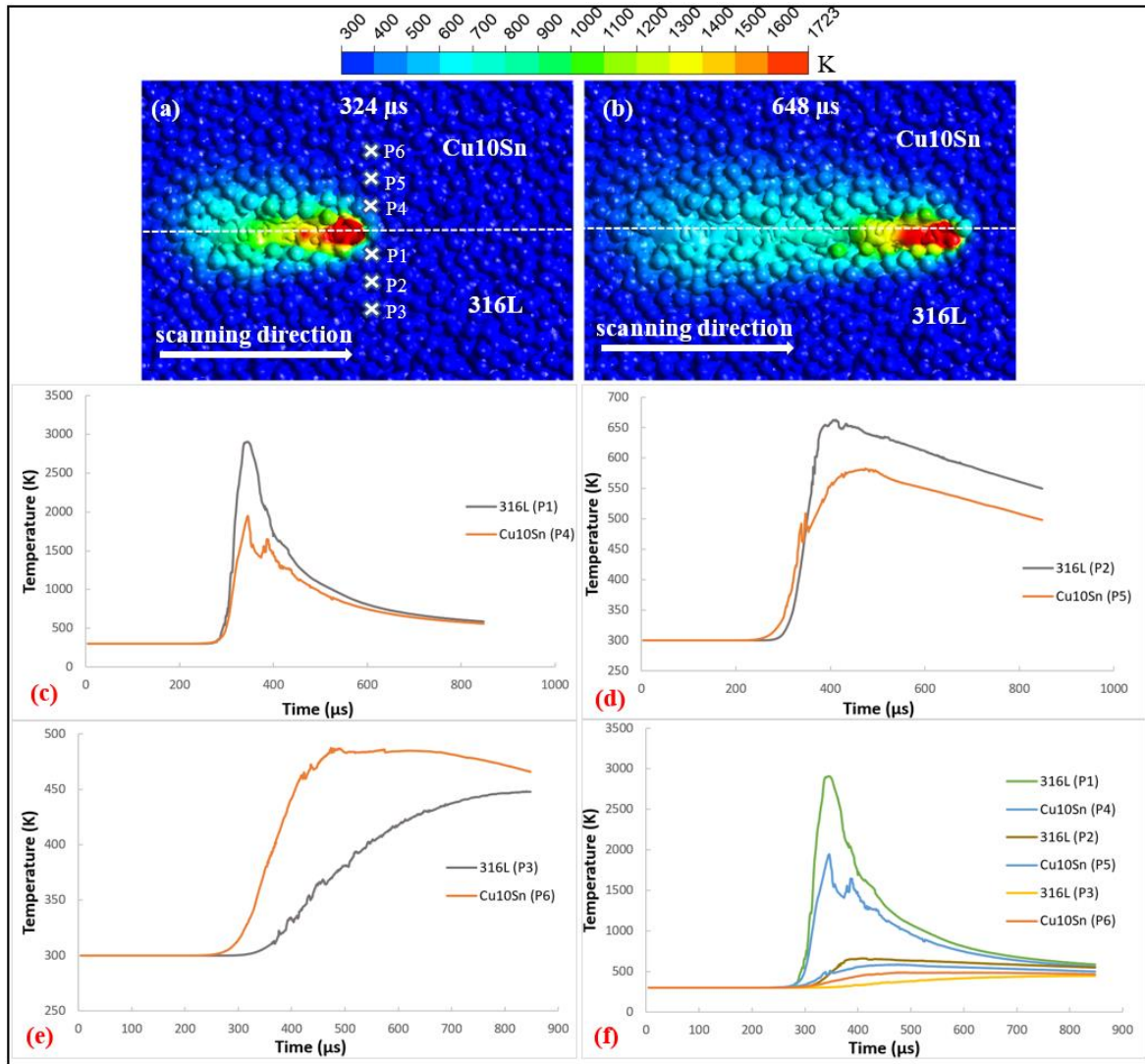
Fig. 14. Temperature distribution of the powder bed at (a) 324 µs, (b) 648 µs, (c-f) comparison of temperature development history of the six points
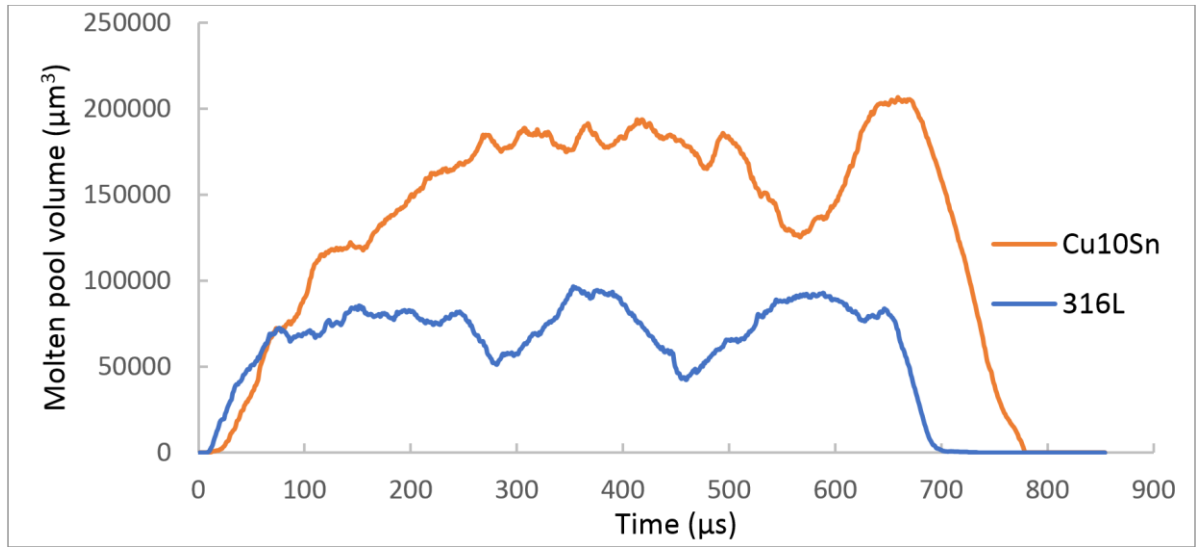
Fig. 15. Molten pool development history of Cu10Sn and 316L
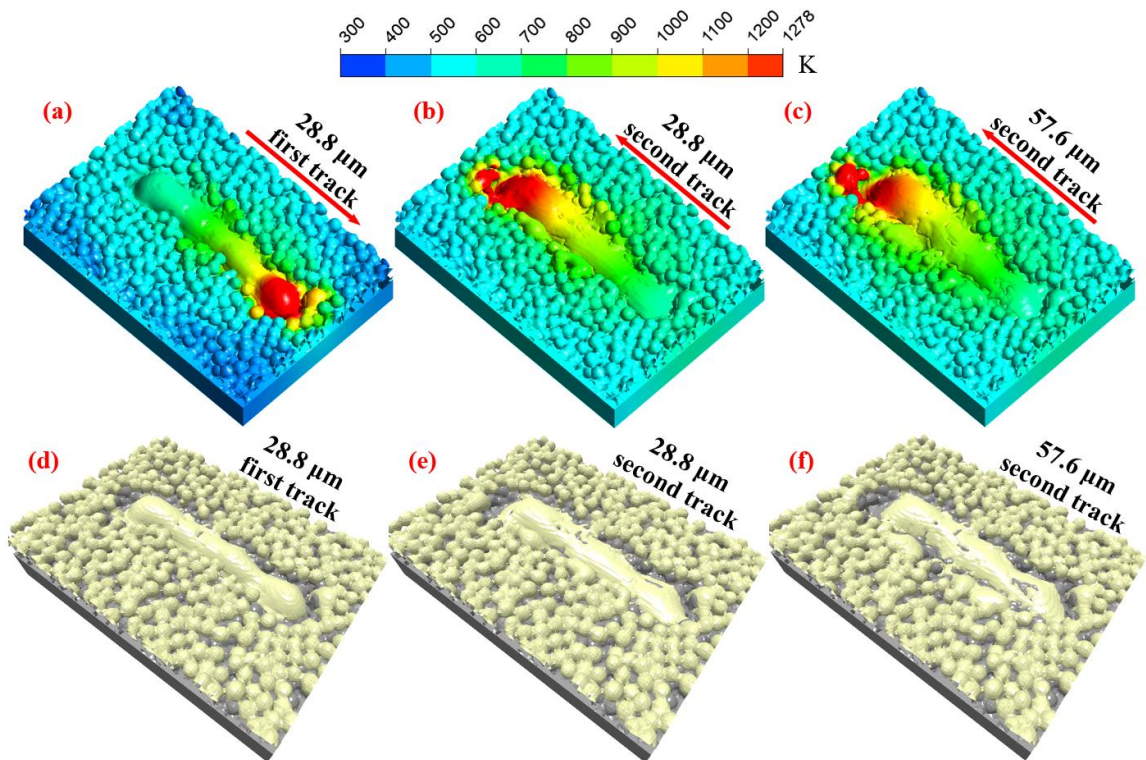
Fig. 16. (a) first track with 28.8 μm hatch spacing, (b) second track with 28.8 μm hatch spacing, (c) second track with 57.6 μm hatch spacing, (d-f) track morphology after solidification
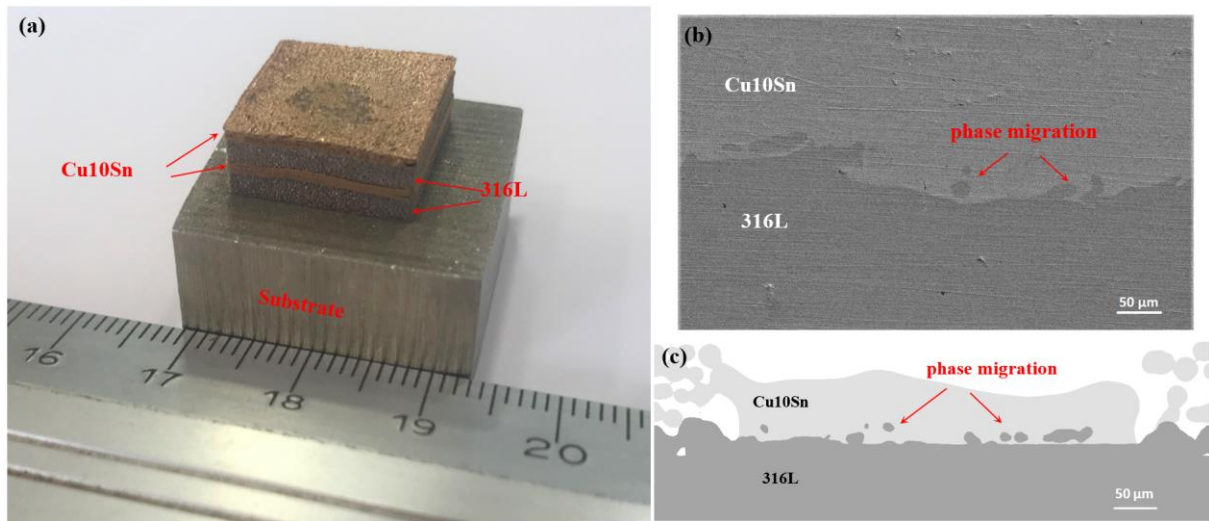
Fig. 17. (a) A 3D printed component produced by a multi-material SLM system, (b) SEM image of the interface between 316L and Cu10Sn, (c) simulated cross-section of the interface
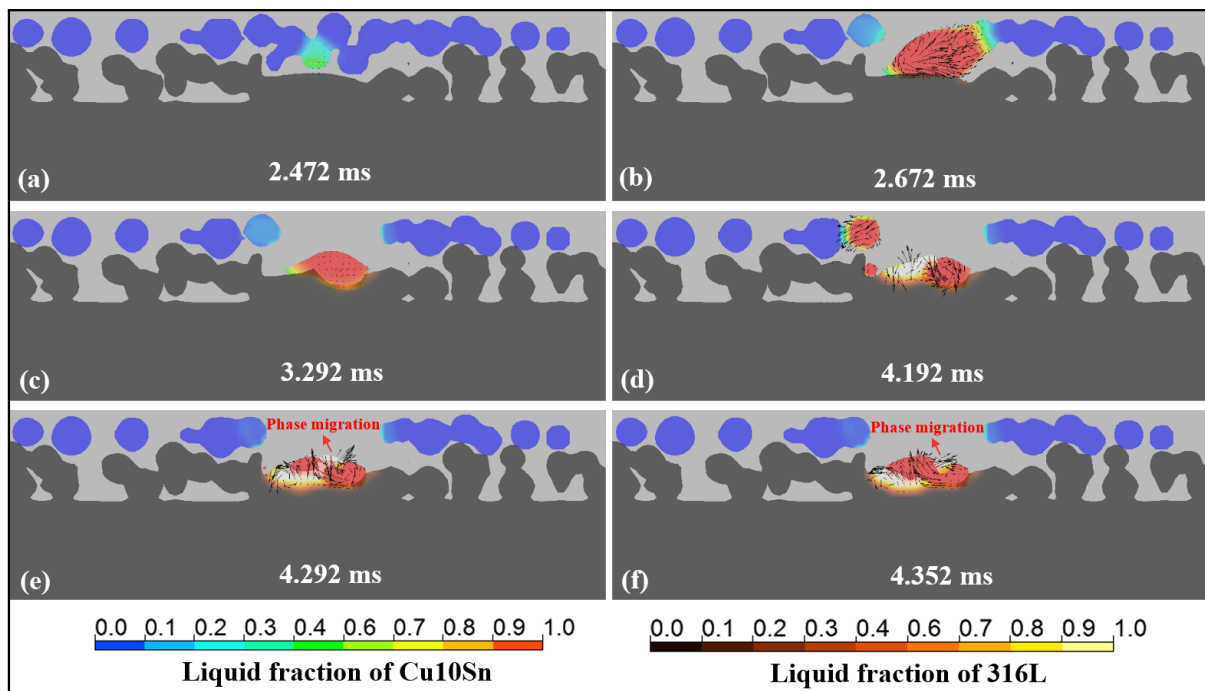
Fig. 18. Molten pool development and phase migration

Table

Table 1 Thermal properties of 316L and Cu10Sn [12, 23, 53, 54, 55]

Symbol	Nomenclature	316L	Cu10Sn
ρ_s	Solidus density (kg·m^{-3})	7980	8780
ρ_l	Liquidus density (kg·m^{-3})	7200	7700
T_s	Solidus temperature (K)	1658	1053
T_l	Liquidus temperature (K)	1723	1278
μ	Viscosity of liquid metal (kg·m^{-1}·s^{-1})	$10^{(2358.2/T-3.5958)}$	0.00225
k_s	Thermal conductivity of solid (W·m^{-1}·K^{-1})	9.248+0.01571T	46
k_l	Thermal conductivity of liquid (W·m^{-1}·K^{-1})	12.41+0.003279T	64
L_m	Latent heat of melting (J·kg^{-1})	2.7×10^5	1.958×10^5
C_p	Specific heat (J·kg^{-1}·K^{-1})	775	505
σ	Surface tension (kg·s^{-2})	1.6	1.15
dσ/dt	Temperature of surface tension (kg·s^{-2}·K^{-1})	-0.8×10^{-3}	-0.2×10^{-3}
σ_s	Stefan-Boltzmann constant (W·m^{-2}·K^{-4})	5.67×10^{-8}	5.67×10^{-8}
R	Universal gas constant (J·mol^{-1}·K^{-1})	8.314	8.314
η	Laser beam absorptivity	0.35	0.03